# Temporal characteristics of backscattered light from a KrF laser-produced plasma

M. Fujita, A. A. Offenberger, and C. E. Capjack
*Department of Electrical Engineering, University of Alberta, Edmonton, Alberta, Canada T6G 2G7*
(Received 4 November 1992; revised manuscript received 11 October 1993)

We report measurements of the time-resolved spectra of backscattered light, near the incident laser wavelength (0.25 $\mu$m), from aluminum plasmas produced by nanosecond pulse KrF laser radiation at an intensity $\simeq 10^{14}$ W/cm$^2$. The redshifted scattered light shows the characteristic temporal and spectral features of stimulated Brillouin scattering. The observed spectral linewidth ($\simeq 0.3$ Å) can be accounted for by inhomogeneity in the plasma flow velocity and density. The experimental results are compared with model predictions of the spectral shift using a two-dimensional hydrodynamic simulation computer code (CASTOR). The dynamics of the spectral shift show a strong correlation with the laser pulse shape, indicating the importance of inverse bremsstrahlung absorption for short wavelength laser radiation and heat transport in a highly collisional plasma.

PACS number(s): 52.25.Qt, 52.35.Nx, 52.40.Nk, 52.50.Jm

## I. INTRODUCTION

In recent laser-plasma experiments [1,2], short wavelength lasers ($\lambda < 1$ $\mu$m), especially KrF lasers ($\lambda \simeq 0.25$ $\mu$m), have clearly demonstrated their advantages over long wavelength lasers. These include high energy absorption, low or negligible hot electron production, increased mass ablation rate and pressure, and improved conversion of laser energy to x-rays. These results have motivated extensive investigations of KrF laser-produced plasma [2], including x-ray generation from various $Z$ plasmas [3], hydrodynamics of ion expansion and recombination [4], and laser induced parametric instabilities [5].

In view of the strategic importance of KrF lasers for fusion and other applications, it is of some consequence to understand the dynamics of amplification of instabilities such as stimulated Brillouin and Raman scattering induced by high intensity KrF laser radiation in a high density (i.e., highly collisional) plasma. Through experiments and computer simulations, we have been studying KrF laser generated stimulated Brillouin scattering (SBS) under conditions where plasma hydrodynamics and inhomogeneity determine the interaction physics. Detailed results of measurements and modeling calculations of the SBS reflectivity will be presented in a separate paper. In this paper, we report spectral and temporal measurements of backscattered light near $\lambda_0 = 0.25$ $\mu$m from a solid aluminum target irradiated by a KrF laser beam that illustrate important features of SBS dynamics in inhomogeneous plasma.

The experiments were conducted with nanosecond KrF laser pulses focused to an average intensity $\simeq 10^{14}$ W/cm$^2$. The observed backscattered light in the focal cone showed the characteristic spectral and temporal features of stimulated Brillouin scattering (SBS), i.e., a spectral red shift and rapid rise and fall of pulse with a maximum at the peak of the incident pulse. The measured red shift showed a weak dependence on the laser intensity. As a result of plasma inhomogeneity, the bandwidth of the scattered light was much broader ($\simeq 0.3$ Å) than that of the incident pulse ($2 \times 10^{-4}$ Å). Temporally, both steady and time-varying spectral shifts were observed. Generally, time-varying spectra were observed at higher intensity ($I_L \geq 10^{14}$ W/cm$^2$).

The dynamics of the spectra shift were compared with two-dimensional (2D) hydrodynamic simulation results and laser pulse shape. The temporal variation observed at high laser intensity cannot be explained by the simulation results. It is found that strong inverse bremsstrahlung absorption heating was important in the short wavelength laser-plasma interaction.

## II. EXPERIMENTAL SETUP

Figure 1 shows a schematic diagram of the experimental setup. A 248-nm KrF laser pulse of 2.4 ns full width at half maximum (FWHM) ($\simeq 0.8$-ns rise, $\simeq 1.6$-ns fall) with an energy of $\simeq 1$ J was focused by an 18-cm aspheric doublet quartz lens, giving average intensity $\simeq 10^{14}$ W/cm$^2$ on target. At the focus, 90% (50%) of the total energy was contained in an area of 330 $\mu$m$^2$ (86 $\mu$m$^2$), equivalent to a 20 $\mu$m (11 $\mu$m) diameter spot size. Variation of the laser intensity was obtained by changing the

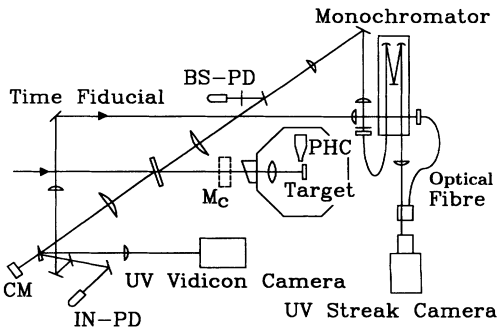


FIG. 1. Schematic diagram of the experimental setup (CM = calorimeter; IN-PD = input photodiode; BS-PD = backscatter photodiode; $M_c$ = removable calibration mirror).

 

laser energy. The laser pulse had a slight temporal modulation—typically 10–20% in amplitude. A solid aluminum plate, oriented at various angles $\theta$ (0°, 22.5°, 45°, and 60°) with respect to the incident laser beam, was used as a target. For a planar plasma expansion, the experimentally measured spectrum is expected to show a $\theta$ dependence due to the plasma flow. On the other hand, for a spherical expansion, the influence of $\theta$ may be less important.

Time-resolved spectra were obtained using a monochromator-streak camera combination. The backscattered light collected by the focusing lens was transported to the monochromator ($f=580$ mm) through an optical fibre (length $\simeq 30$ cm). An image of the exit of the monochromator was magnified and relayed to the streak camera (Hamamatsu Model No. C979). A time fiducial was introduced through an optical fiber to the streak camera without frequency dispersion. The position of the laser wavelength $\lambda_0$ was calibrated every few shots by placing a mirror $M_c$ in the beam and introducing a weak energy pulse ($\simeq 50$ mJ). Typical spectra and temporal resolutions, determined by the monochromator, were measured to be 0.2 Å and 200 ps, respectively.

## III. EXPERIMENTAL RESULTS AND DISCUSSION

### A. Time-resolved spectrum

Experimentally, both steady and temporally varying redshift, illustrated in Fig. 2, as well as temporally smooth and pulsating backscattered light were observed. There was no systematic difference in behavior for different angles of incidence. The SBS spectra shown in Fig. 2 are for an Al target with $\theta=22.5°$ and $I_L=4\times10^{13}$ W/cm$^2$ in case (a) and with $\theta=45°$ and $I_L=1.3\times10^{14}$ W/cm$^2$ in case (b). Figure 3 shows intensity plots of the incident (solid line) and spectrally integrated backscattered light (dashed line) along with spectral shift as a function of time. Solid circles and vertical bars represent the mean peak (taken to correspond to the intensity) and FWHM of the spectral sift. Figures 3(a) and 3(b) correspond to the data shown in Figs. 2(a) and 2(b), respectively. The experimental width of the spectrum was typically 0.5 Å, which included an instrument width of 0.2 Å. The rate for the dynamic spectral redshift in Fig. 3 is approximately 1 Å/ns.

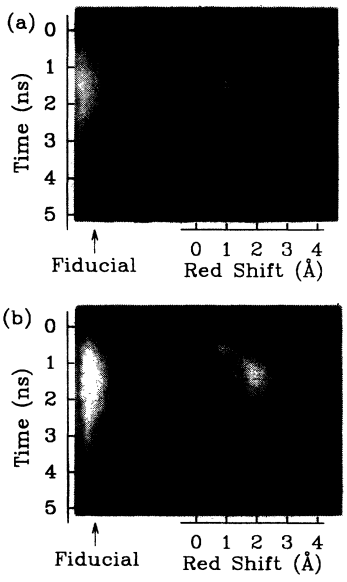


FIG. 2. Typical time-resolved spectra for Al targets. Examples of steady spectral shift (a) with $\theta=22.5°$ and $I_L=4\times10^{13}$ W/cm$^2$ and temporally varying spectral shift (b) with $\theta=45°$ and $I_L=1.3\times10^{14}$ W/cm$^2$.

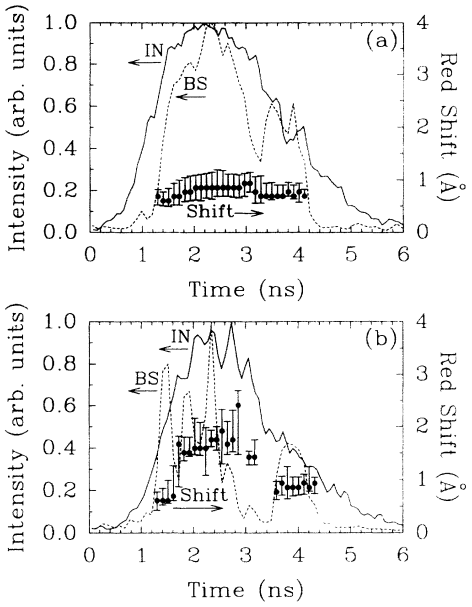


FIG. 3. Intensity plots of incident (solid line) and backscattered light (dashed line) and the spectral shift (solid circles) as a function of time as obtained from Fig. 2.

General features of the time-resolved spectra for oblique incidence included the following: (i) the peak of backscattered light coincided with the peak of incident light (ii) the largest spectral shift was observed at the peak of the incident light, and (iii) the spectral shift of the peak was always red (only the foot of the spectrum was slightly blue shifted in some cases). It is important to note that the temporal modulations observed in the scattered light were not induced by temporal variations in the incident pulse, since the incident beam profile was temporally quite smooth and uncorrelated with the scattering modulations.

In the case of normal incidence, the backscattered light is a mix of Brillouin scattered light and specular reflection from the critical surface. To illustrate the different behavior of spectrally shifted scattered light and specularly reflected light, Fig. 4 shows the intensity of incident light (solid line), backscattered light at laser wavelength $\lambda_0$ (dotted line), and backscattered light with a spectral shift ($\lambda>\lambda_0$, dashed line) as a function of time for an Al target at 0°. It is noted that the shifted and unshifted components are clearly separated in the spectra so that there is little uncertainty in discriminating between these two components. Significantly, the bandwidth of

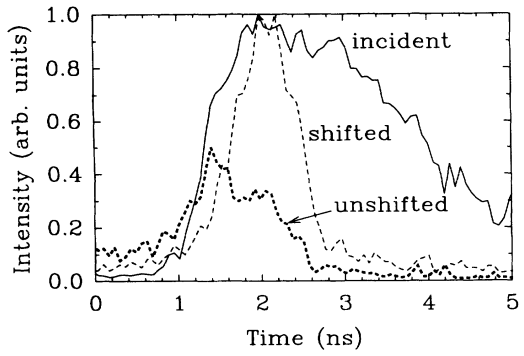


FIG. 4. Intensity plot of incident light (solid line), scattered light at laser wavelength $\lambda_0$ (dotted line), and spectrally shifted scattered light ($\lambda > \lambda_0$, dashed line) as a function of time for Al target at 0° and $I_L = 1.2 \times 10^{14}$ W/cm$^2$. The relative intensity has been normalized independently for a better view; the total reflectivity is 0.15%.

the unshifted component was observed to be the same as that of the incident pulse, whereas the shifted component was spectrally broadened. The measured reflectivity of the unshifted component was ~0.04% compared to ~0.1% for the shifted component. Scattered light at $\lambda_0$ appears only at early time in the laser pulse and starts to decrease well before the peak of the incident pulse. This occurs due to strong inverse bremsstrahlung (IB) absorption of the incident and specularly reflected light in the high density region ($n_e \sim n_c$) when the density scale length becomes comparable to the focal spot size ($t \approx 150$ ps).

Although it is theoretically possible that stimulated Brillouin backscattered light could have a zero spectral shift (Doppler blue shift from plasma flow), we do not expect an SBS contribution to the unshifted component in our case since, in addition to the experimental evidence discussed above, the simulation data indicates a low density ($n_e \sim 0.1-0.2 n_c$) and therefore low SBS growth in the region where plasma flow could cancel the SBS redshift. In addition, the pump intensity and the density scale length are not favorable for the growth of SBS at an early time in the laser pulse.

### B. 2D hydrodynamic simulation

In order to interpret the experimental data, several hydrodynamic simulations were performed. The simulation code used was the two-dimensional cylindrically symmetric Eulerian-plasma hydrodynamic computer code named CASTOR [6]. A nonuniform 75×150 grid was used in the simulations to represent a spatial region of 50 $\mu$m in the radial direction and 200 $\mu$m in the $Z$ direction (direction of laser propagation). The laser routine in CASTOR takes into account laser absorption, diffraction, and refraction. The heat flux is taken to be limited free streaming with flux limiter $f = 0.08$. Here, we present CASTOR results for an Al target with laser energy = 0.5 J, average intensity $= 5.5 \times 10^{13}$ W/cm$^2$, and a focal spot size (90% energy) radius $r_{90\%} = 11$ $\mu$m.

Figure 5 shows contour plots of (a) laser intensity, (b) electron temperature $T_e$, and (c) $\log_{10}(n_e/n_c)$, where $n_e$ and $n_c$ are electron density and the critical density, respectively [$n_c = m_e \omega_0^2/(4\pi e^2)$, $m_e$ is electron mass, $\omega_0$ is laser frequency, and $e$ is electron charge]. These snapshots were taken at 2.0 ns (0.2 ns before the laser peak). The laser beam propagates in the positive $Z$ direction (from bottom to top). The critical surface occurs inside the initial target surface, because of (i) the high critical density for the 0.25-$\mu$m laser wavelength ($n_c = 1.8 \times 10^{22}$ cm$^{-3}$, which is about one-fourth of the solid density of aluminum) and (ii) the large mass ablation rate for short wavelength laser radiation [2]. Due to plasma refraction of the laser beam during the early phase of the plasma formation, an underdense plasma ($n_e < 0.1 n_c$) is created over a wide region (larger than $r_{90\%}$). At later times (as in Fig. 5), the plasma is sufficiently large and uniform so that laser beam refraction by the plasma is small. The electron temperature contour shows that plasma heating is confined to the region of maximum intensity at these later times. This is a consequence of the short electron-ion mean free path $\lambda_{ei}$, which is in the range of 0.2–1 $\mu$m. The late time plasma pressure and

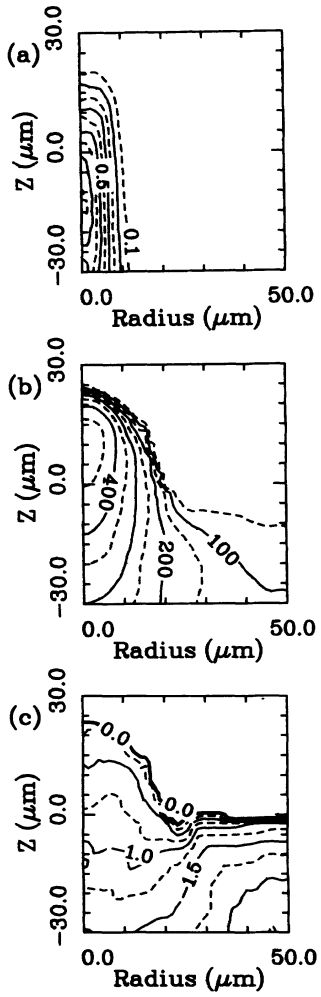


FIG. 5. Contour plots of (a) laser intensity, (b) electron temperature, and (c) $\log_{10}(n_e/n_c)$ at time = 2.0 ns calculated using 2D computer code CASTOR for $I_L = 5.5 \times 10^{13}$ W/cm$^2$.

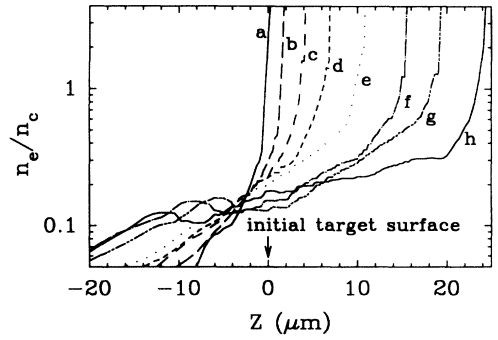


FIG. 6. Calculated temporal evolution of $n_e/n_c$ at $R=0$; $t=0.2$ ns (a), 0.5 ns (b), 0.8 ns (c), 1.0 ns (d), 1.3 ns (e), 1.5 ns (f), 1.8 ns (g) and 2.0 ns (h).

flow velocity are found to be nearly spherical in the simulation data as a result of large $\nabla n$ axially and $\nabla T$ radially in the focal region.

The temporal features of $n_e$ and $T_e$ are presented in Figs. 6 and 7. Figure 6 shows the temporal evolution of electron density profile on laser axis ($R=0$). The symbols a–h denote time $t=0.2$ ns (a), 0.5 ns (b), 0.8 ns (c), 1.0 ns (d), 1.3 ns (e), 1.5 ns (f), 1.7 ns (g), and 2.0 ns (h), respectively. The density profile is steady for $t>1.5$ ns, as expected for spherical plasma expansion with a small focus (i.e., focal spot smaller than sound velocity times laser pulse width $c_s\tau\simeq 100$ μm). It is also noted that the critical density moves away from the laser. Figure 7 shows the maximum calculated electron temperature on axis ($R=0$) as a function of time (solid circles). The solid curve indicates the analytical scaling of temperature with intensity ($T_e\propto I_L^{0.44}$) expected from the self-regulating model [7] for spherical steady plasma. The simulation data fits well to the expected scaling.

In summary, notable features of tightly focused KrF laser-produced plasmas include (i) large target ablation, (ii) spherical expansion for $t>$ (focus size)$/c_s$, (iii) a steady density profile determined by the focal spot size and, (iv) localized plasma heating due to strong inverse bremsstrahlung (IB) absorption and short $\lambda_{ei}$ in the high density plasma.

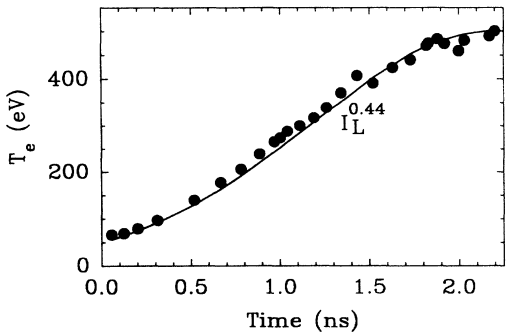


FIG. 7. Calculated maximum electron temperature as a function of time at $R=0$ (solid circles). The solid curve corresponds to a relative laser intensity scaling of $I_L^{0.44}$.

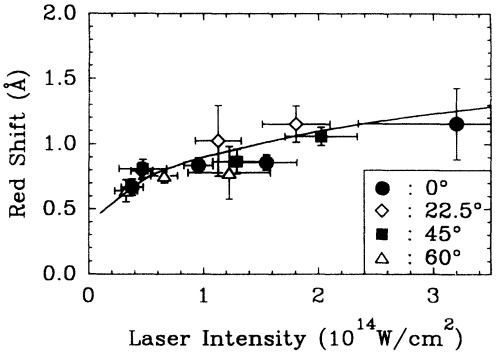


FIG. 8. Spectral shift measured at peak backscattering for various angles of incidence. The solid corresponds to a relative laser intensity scaling of $I_L^{2/9}$.

### C. Spectral shift at peak backscattering

The spectral shift at the peak of backscattering was measured from the time-resolved spectra. Figure 8 shows these spectral shifts as a function of laser intensity for various angles of incidence. A modest increase in redshift was observed with increasing laser intensity, but no significant dependence on $\theta$ was observed. This is expected for spherical plasma expansion. The solid curve shows a relative wavelength scaling of $I^{2/9}$ which would be expected from the scaling of temperature with intensity according to the self-regulating model.

The SBS spectral shift $\Delta\lambda$ in a flowing spherical plasma is given by [8]

$$\frac{\Delta\lambda}{\lambda_0}=2\frac{c_s}{c}\left[1-\frac{n_e}{n_c}\right]^{1/2}(1-M)\,, \tag{1}$$

where $c$ is the speed of light and $M$ is the Mach number. For scattering from a stationary Al plasma with $T_e\simeq 600$ eV (CASTOR data) and $n_e/n_c\simeq 0.4$, the calculated redshift is 2.5 Å (for $T_e=600$ eV and an exponential density scale length of 20 μm, the homogeneous growth rate has a peak near $n_e/n_c\simeq 0.4$, a consequence of gain and inverse bremsstrahlung absorption both increasing with density). The measured redshift of $1.0\pm 0.5$ Å can be explained by taking into account a subsonic plasma flow with an effective $M\simeq 0.6$. These numbers agree well with the CASTOR predictions and interpretation of bandwidth measurements to be discussed in Sec. III D.

Other mechanisms that may produce spectral shifts in scattered light from plasma [9] are not expected to be important here. From the CASTOR data, the predicted redshift for reflection from the critical surface is 0.33 Å which cannot explain the observed redshift of $\simeq 1$ Å. Likewise, the change in optical path between the observer and the reflecting surface due to time-varying density of the moving plasma should have a negligible effect on frequency shift since the density profile becomes steady before the peak of SBS backscatter.

### D. Bandwidth

From the time-resolved spectrum, the (FWHM) linewidth of the SBS spectrum was measured to be typi-

cally 0.5 Å (which includes an instrumental width of 0.2 Å). Assuming a Lorentzian profile, the net linewidth would be 0.3 Å ($\Delta\nu \simeq 1.5\times10^{11}$ 1/s). This value can be compared to the ion acoustic damping rate $\gamma_s$. We use the semi collisional damping rate [10] for $\gamma_s$, since $k_s\lambda_{ii}<1$ in our plasma (where $k_s$ is the wave number of the ion wave and $\lambda_{ii}$ is the ion-ion collision mean free path). The typical ion acoustic wave damping $\gamma_s$ is about $1.3\times10^{11}$ (1/s) which is of the order of the observed bandwidth. Therefore, it is necessary to calculate the detailed SBS spectral shape by using the frequency dependent kinetic growth rate $\gamma_k$ (see Ref. [11]). Although $\gamma_k$ was originally derived for collisionless Landau damping, we compare the semi collisional $\gamma_s^C$ to Landau damping $\gamma_s^L$ as an effective damping rate. For our Al plasma case, we estimate $ZT_e/T_i \simeq 11$ ($\beta=3.3$ in Ref. [11]) which corresponds to $\gamma_s^L=2.2\times10^{11}$ (1/s). It is clear that Landau damping (which gives larger $\gamma_s$ than the collisional damping in our case) would predict narrow spectral shapes (FWHM of the spectrum much less than peak of the spectral shift). Experimentally, such spectral shapes were not observed. Clearly, line broadening due to ion wave damping alone is not enough to explain the linewidth, implying other effects are important.

Spatially inhomogeneous plasma conditions are a likely cause of line broadening, i.e., the observed spectral width is a consequence of SBS contributions from different spatial positions (with varying flow velocity and density). From Eq. (1), the spectral shift dependence on spatial inhomogeneity of temperature, density, and the Mach number can be easily derived, giving

$$\frac{\Delta}{\Delta x}\left[\frac{\Delta\lambda}{\lambda_0}\right]=\frac{c_s}{c}\left[1-\frac{n_e}{n_c}\right]^{1/2}\left[\frac{\Delta T/\Delta x}{T}-\frac{(\Delta n_e/n_c)/\Delta x}{(1-n_e/n_c)}(1-M)-2\Delta M/\Delta x\right]. \tag{2}$$

Here, $T=T_e=T_i$, $k_s\lambda_D \ll 1$, $\Delta T/\Delta x \equiv \partial T/\partial x \simeq T/L_T$ was assumed. For $c_s/c=5.7\times10^{-4}$ ($T=600$ eV, $Z=11$), $n_e/n_c=0.4$, and $M=0.6$, the SBS spectral linewidth $\lambda_w$ is estimated by

$$\lambda_w(\text{Å})=1.1\left[\frac{\Delta T}{T}-0.67\frac{\Delta n_e}{n_c}-2\Delta M\right], \tag{3}$$

where $\Delta M=\Delta v_p/c_s$ and $v_p$ is the plasma flow velocity.

For each term to individually account for $\lambda_w=0.3$ Å, Eq. (5) would require $\Delta T/T\simeq0.3$, $\Delta n_e/n_c\simeq0.4$, or $\Delta M\simeq0.14$. This implies that if $\Delta T$ is the main cause of the line broadening, SBS must be generated over a region where temperature changes from 500 eV (or 400 eV) to 700 eV (600 eV). This is unlikely, since (i) we expect high thermal conductivity in the coronal plasma and (ii) CASTOR data show temperature variations of $\pm100$ eV over 30 $\mu$m in the axial direction and 15 $\mu$m in the lateral direction, larger than the expected SBS gain region. In fact, pump absorption due to inverse bremsstrahlung is so strong in short wavelength laser-produced plasmas that the absorption length is about 10 $\mu$m for $n_e/n_c=0.4$ and $T=600$ eV. Similarly, if $\Delta n_e$ dominates, SBS would have to arise from a region varying from $n_e/n_c=0.2$ to 0.6. This is also unlikely, since CASTOR data show Mach numbers for $n_e/n_c=0.2$ and 0.6 are 1.3 (supersonic) and 0.4 (subsonic) which could cause line broadening $\simeq1.5$ Å (much larger than 0.3 Å). Hence $\Delta n_e/n_c$ alone cannot explain the broadening ($\simeq0.3$ Å). Finally, if $\Delta M$ dominates, it would have to range from 0.53 to 0.67. The variation in flow velocity is therefore a plausible source of the observed broadening.

The plasma parameters deduced above agree with those derived from SBS reflectivity calculations using the experimentally measured laser intensity distribution in the focal plane (a "hot spot" region accounting for $\approx6\%$ of the beam energy with an intensity of 3.8 $I_{\text{av}}$, a medium fluence region accounting for 34% of the beam energy with intensity 2.3 $I_{\text{av}}$ and a background region with intensity 0.7 $I_{\text{av}}$, where $I_{\text{av}}$ is defined by the focal spot area containing 90% of the beam energy). Detailed calculations identify the medium intensity region as the principal contributor to SBS reflectivity with scattering originating from densities ranging from $0.4n_c$ to $0.5n_c$ and flow velocities from $0.55c_s$ to $0.65c_s$.

### E. Temporal features of spectra: $d\lambda/dt$

Since the dynamics of stimulated backscattering are important but not well understood experimentally, we present and discuss the KrF laser-target data for the practical case of solid target irradiation. Recent measurements by Young *et al.* [12] have considered the dynamics of SBS under well-controlled plasma conditions (thin exploding foil with flat-top pulse). Our data indicate that standard hydrodynamic models are inadequate to account for the dynamics of SBS in the case of massive solid targets.

Figure 9 shows $d\lambda/dt$ as a function of laser intensity,

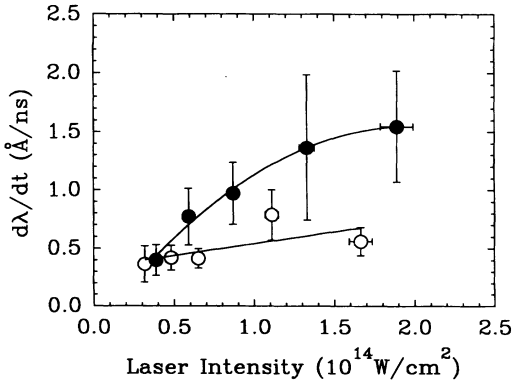


FIG. 9. Temporal change of spectral shift $d\lambda/dt$ as a function of laser intensity. Solid and open circles show positive slope (increasing redshift in time) and absolute value of negative slope (decreasing redshift in time).

obtained by manually fitting a straight line to the increasing and decreasing portions of the time-resolved spectra. Each data point is an average of at least five and typically ten individual measurements; error bars are the standard error in the measured data. The steady spectral shift was regarded as zero slope and included in the data. Since the spectral shift at peak backscattering showed no significant dependence on $\theta$, the data at all angles was averaged. The negative slope values were always smaller than the positive slope which correlates with our laser pulse shape (fast rise and slow fall), giving more rapid change of plasma conditions at an early time. The positive slope was generally observed on the leading part of the laser pulse.

If one estimates the rate of spectral shift from Eq. (2), assuming a steady state density profile and $\Delta v_p$ proportional to $\Delta c_s$, then to lowest order, $\Delta\lambda/\Delta t \simeq 0$. Therefore, it is necessary to examine the hydrodynamic simulation data in detail. Figure 10 shows a comparison of spectral shift dynamics between the experimental and simulation data. The solid and dashed lines are CASTOR data at $n_e/n_c=0.4$ for $I_L=1.1\times10^{14}$ W/cm$^2$ and $5.5\times10^{13}$ W/cm$^2$, respectively; the experimental redshifts (steady and time-varying) are for Al targets at $I_L=3.8\times10^{13}$ W/cm$^2$ and $1.3\times10^{14}$ W/cm$^2$ (see Fig. 2). The steady redshift ($+d\lambda/dt \leq 0.5$ Å/ns) fits well with the simulation data, whereas the time-varying redshift ($+d\lambda/dt \simeq 1.8$ Å/ns) cannot be explained by the simulation results.

Since the general trends of the positive and negative $d\lambda/dt$ correlate with the fast rise and slow fall of the laser pulse, it is also instructive to compare the temporal spectral shift with laser pulse shape $I(t)$ as shown in Fig. 11. The open and solid circles are two examples of typical experimental data for low (a), medium (b), and high (c) laser intensity irradiation. The solid lines show the relative scaling with laser intensity $I_L^{0.22}$ and are normalized to fit the data at the peak of the laser pulse. The laser pulse shape $I_L(t)$ is modeled by a double Gaussian profile with rising and falling HWHM (half width at half maximum) of 0.8 and 1.6 ns, respectively. Only the experimental data for low intensity irradiation fits well to the scaling $I_L^{0.22}$. For higher intensity irradiation, the dependence on $I_L$ seems to be stronger.

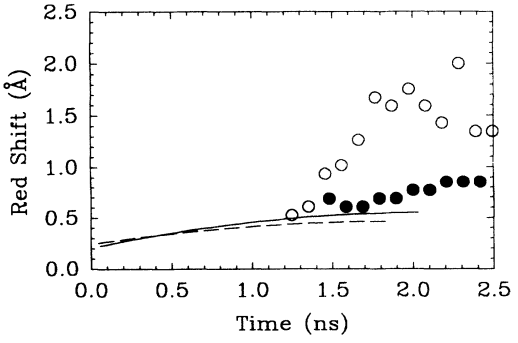


FIG. 10. Comparison of dynamics of redshift between simulation and experimental data. The solid and dashed lines are CASTOR data for $I_L=1\times10^{14}$ and $5.5\times10^{13}$ W/cm$^2$ at $n_e/n_c=0.4$. The solid and open circles show two types of spectral shift observed at $I_L=3.8\times10^{13}$ W/cm$^2$ and $1.3\times10^{14}$ W/cm$^2$ in the experiment, respectively.

Since the CASTOR data show that temporal evolution of electron temperature fits well to the scaling of $I_L(t)^{0.44}$, the spectral shift is expected to follow the scaling of $I_L(t)^{0.22}$. In order to explain the stronger dependence, one would have to assume (i) plasma flow decreasing in time or no plasma flow ($\Delta M/\Delta t \leq 0$), or (ii) localized plasma heating implying that thermal transport is strongly inhibited. The first situation may arise from high intensity hotspots in the laser beam penetrating into higher density plasma where the flow is steady or negative. From CASTOR data with $\Delta n_e/\Delta t=\Delta M/\Delta t=0$, $\Delta\lambda/\Delta t$ is calculated to be 0.6 Å/ns at $t=1.5$–$2.0$ ns. The second possibility is a consequence of the short electron-ion collision mean free path $\lambda_{ei}$ in KrF laser-produced plasma, which is of the order of 0.5 $\mu$m.

Filamentation is not expected to be significant in this experiment. For the KrF laser produced plasma with $I_L \approx 10^{14}$ W/cm$^2$, thermal should dominate over ponderomotive filamentation; the threshold, based on a simple homogeneous theory [13], is well above the laser intensity in our experiments. Even allowing for hotspots in the beam (roughly 2 $\mu$m scalelength and intensity 2.3 times the average intensity) and nonlocal thermal transport [14], thermal filamentation requires a growth length of 5 $\mu$m for the 2 $\mu$m scale perturbation at density $n_e/n_c \sim 0.5$. As seen in Fig. 6, the density scale length in the higher density region is comparable to or shorter than the required growth length. Moreover, strong in-

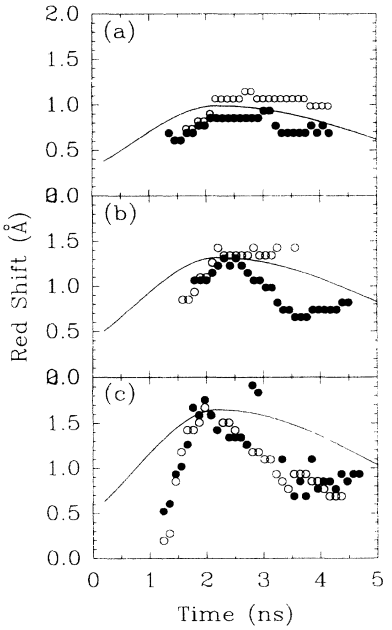


FIG. 11. Typical redshift as a function of time observed in the experiment (solid and open circles) for various laser intensity irradiations. The laser intensities and rates of spectral shift (positive slope) for the experimental data are $4\times10^{13}$ W/cm$^2$ and 0.5 Å/ns (a), $(7\pm3)\times10^{13}$ W/cm$^2$ and 0.8 Å/ns (b), and $(1.5\pm0.3)\times10^{14}$ W/cm$^2$ and 2.0 Å/ns (c). The calculated curves (solid lines) correspond to a relative laser intensity scaling of $I_L(t)^{0.22}$.

verse bremsstrahlung absorption would inhibit growth of the filament.

## IV. CONCLUSIONS

Time-resolved spectral measurements of the backscattered radiation near the laser wavelength ($\lambda_0=0.25$ $\mu$m) from aluminum plasmas created by nanosecond KrF laser pulses have shown stimulated Brillouin scattering to be the principal source of the, albeit weak, reflected light. The magnitude of the spectral shift is consistent with stimulated scattering from a subsonic flowing plasma with average Mach number $M\approx 0.6$ and density $n_e\approx 0.4 n_c$. At the same time, the spectral linewidth can be accounted for by spatial inhomogeneities in the plasma flow velocity, $M=0.55-0.65$, and density, $n_e=(0.4-0.5)n_c$. Time-varying spectral shifts were observed at higher laser intensities. The dynamics of the spectral shift at high laser intensity showed a strong correlation with the laser pulse shape which could not be explained by 2D hydrodynamic predictions based on standard heat transport models. More detailed hydrodynamic simulations with nonlocal heat transport models as well as simultaneous calculation of the backscattered light in the laser propagation routines are probably required to accurately interpret the time-varying spectra.

## ACKNOWLEDGMENTS

The authors gratefully acknowledge the technical assistance of B. Harwood and A. Haromy. We wish to express appreciation to Dr. Vick for assistance with CASTOR simulations and to Dr. Rozmus, Dr. Tikhonchuk, and Dr. Fedosejevs for valuable discussions. This work was supported by the Natural Sciences and Engineering Research Council of Canada.

[1] W. Seka, R. S. Craxton, J. Delettrez, L. Goldman, R. Keck, R. L. McCrory, D. Shvarts, J. M. Soures, and R. Boni, Opt. Commun. **40**, 437 (1982).

[2] A. A. Offenberger, R Fedosejevs, P. D. Gupta, R. Popil, and Y. Y. Tsui, Laser Part. Beams **4**, 329 (1986).

[3] R. Popil, P. D. Gupta, R. Fedosejevs, and A. A. Offenberger, Phys. Rev. A **35**, 3874 (1987); P. D. Gupta, R. Popil, R. Fedosejevs, A. A. Offenberger, D. Saltzmann, and C. E. Capjack, Appl. Phys. Lett. **48**, 103 (1986).

[4] P. D. Gupta, Y. Y. Tsui, R. Popil, R. Fedosejevs, and A. A. Offenberger, Phys. Rev. A **34**, 4103 (1986).

[5] A. A. Offenberger, J. Santiago, M. Fujita, R. Fedosejevs, and W. Rozmus, Laser Part. Beams **8**, 153 (1990).

[6] J. P. Christiansen and N. K. Winsor, Comput. Phys. Commun. **17**, 397 (1979); R. Rankin, R. Marchand, and C E. Capjack, Phys. Fluids **31**, 2327 (1988).

[7] P. Mora, Phys. Fluids **25**, 1051 (1982); F. Dahmani and T. Kerdja, Phys. Fluids B **3**, 1232 (1991).

[8] T. W. Johnston, G. R. Mitchel, and B. Grek, Phys. Fluids **25**, 179 (1982).

[9] T. Dewandre, J. R. Albritton, and E. A. Williams, Phys. Fluids **24**, 528 (1981).

[10] M. Casanova, Laser Part. Beams **7**, 165 (1989).

[11] A. A. Offenberger, M. R. Cervenan, A. M. Yam, and A. W. Pasternak, J. Appl. Phys. **47**, 1451 (1976).

[12] P. E. Young, R. L. Berger, and K. G. Estabrook, Phys. Fluids B **4**, 2605 (1992).

[13] W. L. Kruer, Comments Plasma Phys. Controlled Fusion **9**, 63 (1985).

[14] E. M. Epperlein, Phys. Rev. Lett. **65**, 2145 (1990).

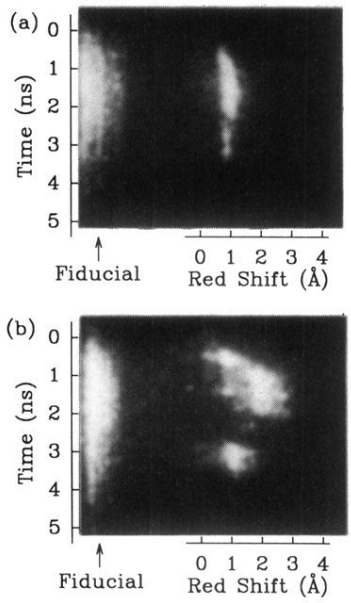


FIG. 2. Typical time-resolved spectra for Al targets. Examples of steady spectral shift (a) with $\theta=22.5°$ and $I_L=4\times10^{13}$ W/cm$^2$ and temporally varying spectral shift (b) with $\theta=45°$ and $I_L=1.3\times10^{14}$ W/cm$^2$.